

Ultralong nitrogen/sulfur Co-doped carbon nano-hollow-sphere chains with encapsulated cobalt nanoparticles for highly efficient oxygen electrocatalysis

Wei Zhang^{1,2,3} | Xingmei Guo³ | Cong Li¹ | Jiang-Yan Xue¹ |
Wan-Ying Xu¹ | Zheng Niu¹ | Hongwei Gu¹ | Carl Redshaw⁴ |
Jian-Ping Lang^{1,2} 

¹College of Chemistry, Chemical Engineering and Materials Science, Soochow University, Suzhou, People's Republic of China

²State Key Laboratory of Organometallic Chemistry, Shanghai Institute of Organic Chemistry, Chinese Academy of Sciences, Shanghai, People's Republic of China

³College of Environmental and Chemical Engineering, Jiangsu University of Science and Technology, Zhenjiang, People's Republic of China

⁴Department of Chemistry, University of Hull, Hull, UK

Correspondence

Xingmei Guo, College of Environmental and Chemical Engineering, Jiangsu University of Science and Technology, Zhenjiang, 212003, People's Republic of China.

Email: guoxm@just.edu.cn

Carl Redshaw, Department of Chemistry, University of Hull, Hull JU6 7RX, UK.

Email: C.Redshaw@hull.ac.uk

Jian-Ping Lang, College of Chemistry, Chemical Engineering and Materials Science, Soochow University, Suzhou, 215123, People's Republic of China.

Email: jplang@suda.edu.cn

Funding information

Collaborative Innovation Center of Suzhou Nano Science and Technology; National Natural Science Foundation of China, Grant/Award Numbers: 21773163, 22271203; EPSRC for an Overseas Travel Grant, Grant/Award Number: EP/R023816/1; State Key Laboratory of Organometallic Chemistry of Shanghai Institute of Organic Chemistry, Grant/Award Number: KF2021005; Priority Academic Program Development of Jiangsu Higher Education Institutions; Project of Scientific and Technologic Infrastructure of Suzhou, Grant/Award Number: SZS201905

Abstract

The development of simple and effective strategies to prepare electrocatalysts, which possess unique and stable structures comprised of metal/nonmetallic atoms for oxygen reduction reaction (ORR) and oxygen evolution reaction (OER), is currently an urgent issue. Herein, an efficient bifunctional electrocatalyst featured by ultralong N, S-doped carbon nano-hollow-sphere chains about 1300 nm with encapsulated Co nanoparticles (Co-CNHSCs) is developed. The multifunctional catalytic properties of Co together with the heteroatom-induced charge redistribution (i.e., modulating the electronic structure of the active site) result in superior catalytic activities toward OER and ORR in alkaline media. The optimized catalyst Co-CNHSC-3 displays an outstanding electrocatalytic ability for ORR and OER, a high specific capacity of 1023.6 mAh g_{Zn}⁻¹, and excellent reversibility after 80 h at 10 mA cm⁻² in a Zn-air battery system. This work presents a new strategy for the design and synthesis of efficient multifunctional carbon-based catalysts for energy storage and conversion devices.

KEYWORDS

Co nanoparticles, N,S co-doping, oxygen electrocatalysts, rechargeable Zn-air batteries, ultralong carbon nano-hollow-sphere chains

This is an open access article under the terms of the Creative Commons Attribution License, which permits use, distribution and reproduction in any medium, provided the original work is properly cited.

© 2023 The Authors. *Carbon Energy* published by Wenzhou University and John Wiley & Sons Australia, Ltd.

1 | INTRODUCTION

The continued massive consumption of traditional fossil fuels has led to a global energy crisis and severe environmental pollution, which requires us to develop alternative environmentally friendly and efficient energy conversion and storage technologies.^{1,2} Among them, the oxygen reduction reaction (ORR) and the oxygen evolution reaction (OER) are central reactions for new energy conversion and storage technologies such as metal-air batteries.^{3,4} Unfortunately, both the ORR and OER involve multiple electron transfers with sluggish kinetics, which greatly limits the energy conversion efficiency of associated electrochemical devices.⁵⁻⁷ High-performance catalysts are essential to increasing the reaction rate. To date, noble metal-based catalysts (such as Pt, Ir/Ru) have been shown to possess excellent catalytic effects but are limited to specific reactions and are unable to serve as multifunctional electrocatalysts. In addition, their scarcity, cost, and poor durability also greatly hinder any large-scale application of noble metal-based catalysts.⁸⁻¹⁰ As a consequence, the use of high-efficiency and durable nonprecious electrocatalysts is highly desirable.^{11,12}

In recent years, the trend of replacing noble metal catalysts with cheap and durable carbon-based materials doped with nonmetallic atoms has intensified,¹³⁻¹⁶ and various carbon-based materials have been utilized as ORR or OER catalysts, including N-doped carbon nanotubes,¹⁷ S-doped graphene,¹⁸ S, N dual-doped carbon nanosheets,¹⁹ N, P co-doped mesoporous carbon,²⁰ and so forth. On one hand, the carbon material as the substrate has a larger specific surface area, which can expose more active sites; on the other hand, when heteroatoms are introduced into the carbon matrix, special active chemical bonds can be formed, which can induce a charge redistribution and thereby modulate the electronic structure of the active site.^{14,21} Although the surface area significantly affects the electrochemical properties of carbon-based materials, the electronic structure plays the dominant role in controlling the intrinsic catalytic activities.²²⁻²⁴ The primary task of endowing carbon-based materials with specific catalytic activity for ORR/OER is to modulate their electronic structures.^{25,26} In other words, properly modulated electronic structures can improve the interactions between the catalyst surface and generated O intermediates (such as O*, OH*, and OOH*). Liu et al. proved that such interactions need to be of moderate strength; too weak interactions are not conducive to O₂ splitting, while too strong ones make it difficult to desorb O-derived intermediates.²⁷ Unfortunately, compared with noble metal catalysts, the nonmetallic doped catalyst surfaces

still have weak interactions with intermediates, which are not conducive to O–O splitting. However, incorporation of the transition metal Co in the form of nanoparticles (NPs) or/and doping atoms can provide accessible electron density for O₂ to promote O–O splitting, which overcomes the shortcomings of carbonaceous catalysts.²⁸ At present, most of these catalysts are synthesized by pyrolyzing metal-organic framework precursors,^{29,30} which are cumbersome and difficult to scale up. Therefore, it remains a challenge to develop simple and effective strategies for preparing highly efficient transition metal Co/nonmetallic atom-doped carbon catalysts.

In this work, we develop a one-step pyrolysis method to produce intriguing ultralong carbon nano-hollow-sphere chains (CNHSC) with embedded Co NPs (Figure 1). In the synthesis of these chains, CoCl₂ was employed as the metal source, dicyandiamine (DCDA) as the carbon and nitrogen source, and ZnSO₄ as the sulfur source. These components allowed us to utilize the multifunctional catalytic properties of Co together with the facile decomposition of DCDA and vaporization of Zn at higher temperatures to synthesize ultralong N,S co-doped carbon nano-hollow-sphere chains with encapsulated Co NPs (Co-CNHSC) as a bifunctional catalyst for both OER and ORR. To our knowledge, the CNHSC has an unprecedented length of ca. 1300 nm, which is the longest among the known carbon nanosphere chains reported previously. Morphological and compositional characterizations confirmed that some Co atoms grew into metallic nanograins wrapped by CNHSC. Importantly, this configuration significantly modulates the electronic structure and improves the catalytic activity (vide infra). Moreover, the newly synthesized Co-CNHSC-3 catalyst exhibited outstanding catalytic activity for both the OER and ORR. In addition, as a cathode catalyst for Zn-air batteries, the specific capacity and peak power density of Co-CNHSC-3-based devices reached 1023.6 mAh g_{Zn}⁻¹ and 118 mW cm⁻², respectively. After 80 h of continuous charge/discharge cycles, the voltage gap remained almost unchanged, which suggests that this catalyst would be a promising candidate for highly efficient bifunctional oxygen electrocatalysis.

2 | EXPERIMENTAL SECTION

2.1 | Synthesis of Co-CNHSC

In a typical synthesis of Co-CNHSC-1, CoCl₂·6H₂O (0.1 g) and DCDA (2.0 g) were dissolved in 20 mL of deionized water at 60°C. Then, ZnSO₄·7H₂O (0.2 g) was added to

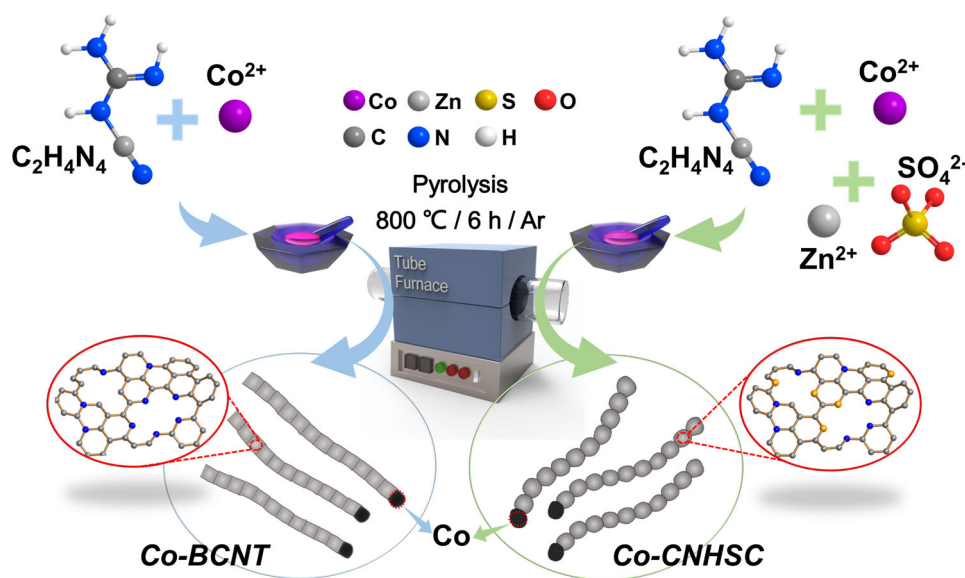


FIGURE 1 Schematic illustration for the synthesis of Co-BCNT and Co-CNHSC

the solution, which was stirred for 10 min and freeze-dried in vacuum for 24 h. After that, the dry solid was placed in a tubular furnace and heated at 800°C with a heating rate of 2°C min⁻¹ for 6 h under an Ar atmosphere to yield the product. A similar workup was used for the synthesis of Co-BCNT-2 (Co/DCDA/Zn-0.2/2/0.2), Co-BCNT-3 (Co/DCDA/Zn-0.2/3/0.2), and Co-BCNT-4 (Co/DCDA/Zn-0.2/3/0.4) by using the different ratios of the three reactants.

2.2 | Synthesis of Co-BCNT

Co-BCNT-1 (Co/DCDA-0.2/2) and Co-BCNT-2 (Co/DCDA-0.2/3) were prepared in a similar way to that used for the synthesis of Co-CNHSC by changing the ratios of CoCl₂·6H₂O/DCDA.

2.3 | Characterization

Scanning electron microscopy (SEM) images and energy-dispersive X-ray spectroscopy (EDS) were obtained with a HITACHI S-4700 cold field emission scanning electron microscope operated at 15 kV. High-resolution transmission electron microscopy (HRTEM), high-angle annular dark field scanning transmission electron microscopy (HAADF-STEM), and elemental mapping were performed on an FEI Tecnai F20 transmission electron microscope at an acceleration voltage of 200 kV. Powder X-ray diffraction (PXRD) was carried out on an X'Pert-Pro MPD diffractometer (Netherlands PANalytical) with a Cu K α

X-ray source ($\lambda = 1.540598 \text{ \AA}$). Raman spectra of the samples were obtained from a LabRAM HR800 confocal Raman microscopic system under an excitation laser of 633 nm. The specific surface area and pore size of the samples were calculated by Brunauer–Emmett–Teller (BET) and Barrett–Joyner–Halenda (BJH) models, respectively. A Fourier transform infrared spectrophotometer (FTIR, Nicolet iS10) was used to detect the functional groups at the surface of the as-prepared samples over a range of 500 to 4000 cm⁻¹ with a resolution of 2 cm⁻¹. The X-ray photoelectron spectrum (XPS) was recorded on an SSI S-Probe XPS spectrometer.

2.4 | Electrode preparation

For the preparation of the working electrode, 5 mg of the catalyst was dispersed in 1 mL of water/isopropanol (1:3 volume ratio) solvent followed by adding 25 μL of Nafion. After sonication for 30 min to form a homogeneous ink, a 10 μL drop was cast on a freshly polished RDGCE/GCE and dried under ambient conditions. Commercial Pt/C (20 wt%) and RuO₂-modified RDGCE/GCE were also prepared under the same procedure for comparative purposes.

2.5 | OER/ORR measurements

To demonstrate the catalytic performance of OER, a three-electrode system was employed with a modified GCE, platinum foil, and Ag/AgCl electrode as working,

auxiliary, and reference electrodes, respectively. The aqueous solution of 1.0 mol L⁻¹ KOH was used as the electrolyte and bubbled by high-purity N₂ for 30 min before testing. Cyclic voltammetry (CV), linear sweep voltammetry (LSV), and chronoamperometry were performed with a CHI 660E electrochemical workstation (Chenhua, Shanghai). The LSV measurement for OER was conducted at a scan rate of 5 mV s⁻¹.

To demonstrate the catalytic performance for ORR, all electrochemical measurements were conducted using a three-electrode system on an Autolab PFSTAT302N electrochemical workstation. A modified rotating disk glassy carbon electrode (RDGCE), platinum plate, and Ag/AgCl electrode were used as working, auxiliary, and reference electrodes, respectively. 0.1 mol L⁻¹ KOH as the electrolyte was bubbled and saturated with nitrogen or oxygen before testing. CV was conducted in both nitrogen and oxygen-saturated electrolytes at a scan rate of 50 mV s⁻¹. LSV was performed in the oxygen-saturated electrolyte at a scan rate of 10 mV s⁻¹ with the rotation speed of RDGCE varied from 400 to 2025 rpm. All potentials were calibrated to a reversible hydrogen electrode (RHE) by adding a value (0.197 + 0.059 × pH). Durability and methanol tolerance were tested by chronoamperometry under 0.6 V versus RHE in oxygen-saturated electrolytes at 1600 rpm. To calculate the electron transfer number (*n*), the slopes of Koutecky–Levich (K–L) plots derived from LSV curves were analyzed based on the following equations³¹:

$$\frac{1}{J} = \frac{1}{J_L} + \frac{1}{J_K} = \frac{1}{B\omega^{1/2}} + \frac{1}{J_K}, \quad (1)$$

$$B = 0.62nFC_0(D_0)^{2/3}\nu^{-1/6}, \quad (2)$$

$$\text{ECSA} = \frac{C_{dl}}{C_s}, \quad (3)$$

where *J* is the measured current density, *J_K* and *J_L* are the kinetic and diffusion limiting current densities, ω is the angular velocity, *n* is the electron transfer number, *F* is the Faraday constant (96,485 C mol⁻¹), *C₀* is the bulk concentration of oxygen (1.2 × 10⁻⁶ mol cm⁻³), *D₀* is the diffusion coefficient of oxygen in 0.1 mol L⁻¹ KOH (1.9 × 10⁻⁵ cm² s⁻¹), and ν is the kinematic viscosity of the 0.1 mol L⁻¹ KOH electrolyte (0.01 cm² s⁻¹). *C_{dl}* is the electric double-layer capacitance calculated from the non-Faradaic region and *C_s* is the specific capacitance of a flat, smooth electrode surface, whose value was numerically taken as 40 μF cm⁻².³² All polarization curves involved in this study were corrected for 80% iR compensation.

2.6 | Liquid Zn-air battery measurements

To prepare the air cathode, 1 mg of Co-CNHSC-3 (or 20 wt.% Pt/C and RuO₂ mixture, Pt/C:RuO₂ = 1:1, weight ratio) was mixed with 0.25 mg of acetylene black and 10 μL of 5 wt.% Nafion solution and dispersed in 0.25 mL of ethanol with the assistance of at least 30 min sonication to form a homogeneous ink. This catalyst ink was uniformly drop cast onto a 1 cm² hydrophobic carbon paper electrode, to achieve a catalyst loading of 1 mg cm⁻², and dried at room temperature. The air cathode was then paired with a polished zinc plate (thickness: 0.3 mm) anode and assembled in a customized electrochemical cell filled with 6 mol L⁻¹ KOH containing 0.2 mol L⁻¹ zinc acetate. The gas diffusion layer has an effective area of 1 cm² and allows O₂ from ambient air to reach the catalyst sites. The as-fabricated Zn-air batteries were characterized under ambient conditions using a LAND CT2001A multichannel battery testing system. The time interval was set as 10 min for the cycle test between each charge and discharge at a current density of 10 mA cm⁻². Polarization data (V–i) were collected with a CHI 660E electrochemical workstation using LSV at a scan rate of 10 mV s⁻¹. The corresponding specific capacity (mAh g_{Zn}⁻¹) and power density (mW cm⁻²) were calculated by the following equations, respectively.³³

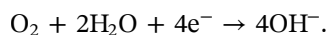
$$\text{Specific capacity} = \frac{\text{current} \times \text{service hours}}{\text{weight of consumed Zn}}, \quad (4)$$

$$\text{Power density} = \frac{\text{average discharge}}{\text{effective area}} \times \text{voltage}. \quad (5)$$

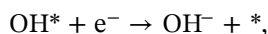
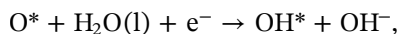
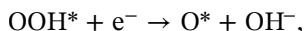
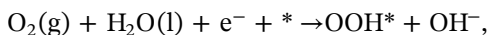
2.7 | Theoretical calculations

We used the density functional theory (DFT) as implemented in the Vienna Ab initio simulation package (VASP) in all calculations. The exchange-correlation potential is described by using the generalized gradient approximation of Perdew–Burke–Ernzerhof (GGA-PBE).³⁴ The projector augmented wave (PAW) method is employed to treat interactions between ion cores and valence electrons.^{35,36} The plane-wave cutoff energy was fixed to 500 eV. Given structural models were relaxed until the Hellmann–Feynman forces smaller than –0.02 eV/Å and the change in energy smaller than 10⁻⁵ eV were attained. During the relaxation, the Brillouin zone was represented by a Γ centered k-point grid of 2 × 3 × 1. Spin polarization was considered in all calculations. To avoid the periodic image interaction between the two nearest neighboring unit cells, the vacuum was set to 20 Å in the z-direction.

The overall ORR in the alkaline environment can be written as³⁷



In our model, we assume that the ORR is processed in the four-electron pathway,



where the symbol * donates an active site on the catalyst. (l) and (g) refer to liquid and gas phases, respectively.

For each step, the reaction free energy ΔG is defined by the following equation³⁸:

$$\Delta G = \Delta E + \Delta \text{ZPE} - T\Delta S + \Delta G_{\text{U}} + \Delta G_{\text{Ph}}. \quad (6)$$

where the ΔE , ΔZPE , and ΔS are the different energy, zero-point energy, and entropy of the reaction, respectively.

3 | RESULTS AND DISCUSSION

As shown in Figure 1, $\text{ZnSO}_4 \cdot 7\text{H}_2\text{O}$ (0.2 g) was mixed with $\text{CoCl}_2 \cdot 6\text{H}_2\text{O}$ (0.1 g) and DCDA (2.0 g) in water. Then, the resulting solution was freeze-dried in vacuo to yield a dry solid, which was pyrolyzed at 800 °C for 6 h

under an argon atmosphere, forming ultralong N,S-doped carbon nano-hollow-sphere chains with encapsulated Co NPs (Co-CNHSC-1). Varying the ratios of the three reactants gave rise to a set of similar samples, which were denoted as Co-CNHSC-2 (Co/DCDA/Zn-0.2/2/0.2), Co-CNHSC-3 (Co/DCDA/Zn-0.2/3/0.2), and Co-CNHSC-4 (Co/DCDA/Zn-0.2/3/0.4). In the absence of $\text{ZnSO}_4 \cdot 7\text{H}_2\text{O}$, similar treatments with $\text{CoCl}_2 \cdot 6\text{H}_2\text{O}$ (0.2 g) and DCDA (2.0–3.0 g) afforded N-doped bamboo-like carbon nanotubes (BCNTs) with encapsulated Co NPs, denoted as Co-BCNT-1 (Co/DCDA-0.2/2) and Co-BCNT-2 (Co/DCDA-0.2/3), respectively. It is noteworthy that the ratio of precursor materials has a significant influence on the sample morphology. In the absence of ZnSO_4 , the as-prepared samples have a BCNT morphology (Figure S1), whose formation mechanism was similar to those described in the literature.^{39,40} However, in the presence of ZnSO_4 , the resulting samples adopt an unprecedented morphology showing an ultralong N,S-doped CNHSC with Co NPs being encapsulated at its tip (Figure S2), which means a different formation mechanism and deserves comment.

To elucidate the possible formation mechanism of such an intriguing chain nanostructure (taking Co-CNHSC-3 as a representative sample), TEM was employed to snapshot the morphology and size of the samples at different pyrolysis temperatures and times. As shown in Figure 2A,B, in the range of 700–750 °C, dicyandiamide is decomposed to produce reducing gas and nitrogen-carbon (CN_x).^{41,42} A small amount of sulfate adsorbed at the surface of the carbon matrix also gets decomposed, further forming the N,S co-doped carbon materials. Meanwhile, Co^{2+} and Zn^{2+} ions are reduced and aggregated into

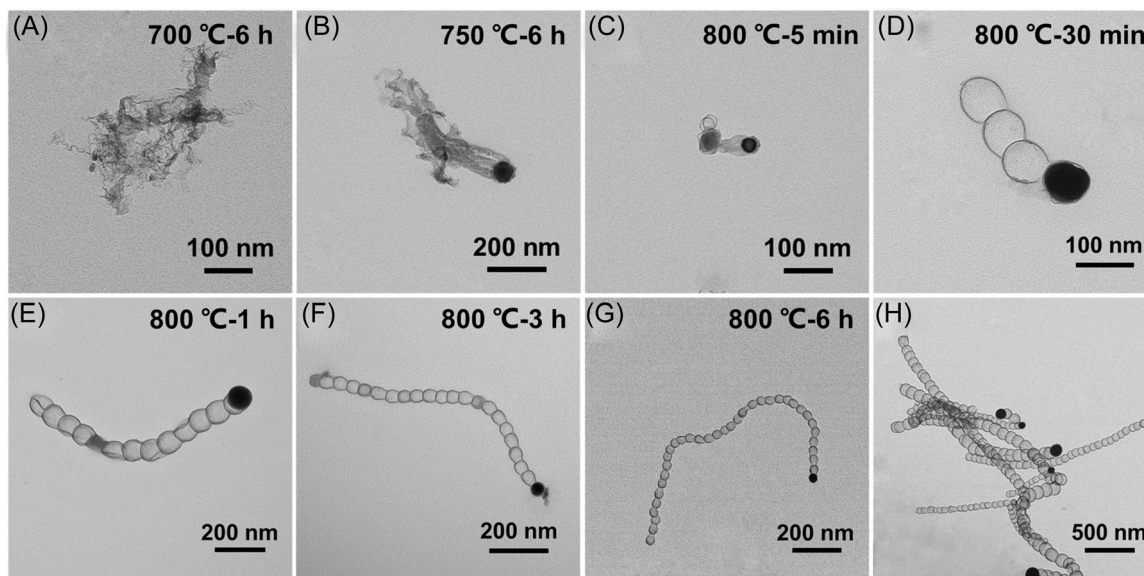


FIGURE 2 (A–G) TEM images of Co-CNHSC with different calcination temperatures and times. (H) TEM image of Co-CNHSC-3.

cobalt-zinc NPs by the reducing gas, which serves as the seeds for the growth of the N,S-doped CNHSCs. After 6 h pyrolysis, no evident long carbon nano-hollow-sphere chains (CNHSCs) are observed. However, when the pyrolysis temperature was raised up to 800°C for 5 min, some carbon nano-hollow-spheres and one enclosing Co NPs appear (Figure 2C). It seems that the above N,S co-doped carbon species become to cover at the surface of alloy NPs to form a N,S-doped carbon sphere layer. After pyrolysis at 800°C for 30 min, a Co-CNHC of three hollow spheres and one solid sphere (alloy NPs inside) with a length of ca. 300 nm is observed (Figure 2D). It is evident that the Co-CNHC gets elongated as the pyrolysis proceeds. This is probably because uneven heating makes part of the zinc in the aggregated cobalt-zinc NPs be vaporized and escaped via the argon gas flow, forming defects on the complete N,S-doped carbon sphere layer (Figure 2E). Such defects further make the cobalt NPs unevenly stressed and force them to move out of the defects to form hollow spheres. This is followed by shrinkage of the graphitic carbon sphere walls driven by energy considerations (Figure S3).³⁹ With the pyrolysis time being prolonged, the number of CNHSCs is gradually increased and the Co-CNHC is continuously lengthened

in an almost ordered fashion. After the pyrolysis for 1 h and 3 h, the chains keep one solid carbon sphere (Co NPs inside) at one of their tips but contain 12 and 20 carbon hollow nanospheres and become ca. 600 nm (Figure 2E) and 900 nm (Figure 2F) long, respectively. Finally, as shown in Figure 2G, an ultralong Co-CNHC consisting of 35 carbon hollow nanospheres and one carbon sphere enclosing Co NPs with a diameter of ca. 30–40 nm and a length of ca. 1300 nm is formed after pyrolysis for 6 h, and the resulting chains stay in a relatively uniform size (Figure 2H). Such a Co-CNHC-3 chain is the longest among the Co-CNHC samples and those reported in the literature. When the zinc source is changed, similar Co-CNHCs are formed, suggesting that the zinc ions play a key role in the formation of the Co-CNHCs (Figure S4). However, such an ultralong string gets collapsed when the pyrolysis continued to go at 800°C for 8 h (Figure S5), which is probably due to the fact that DCDA and the other two reactants are completely consumed and no more carbon source is available for further growing CNHSCs.

Followed by the above formation mechanism study, we employed SEM and HRTEM to further reveal the internal nanostructure of Co-CNHC-3. The SEM images (Figure 3A,B) along with the TEM image (Figure 3C)

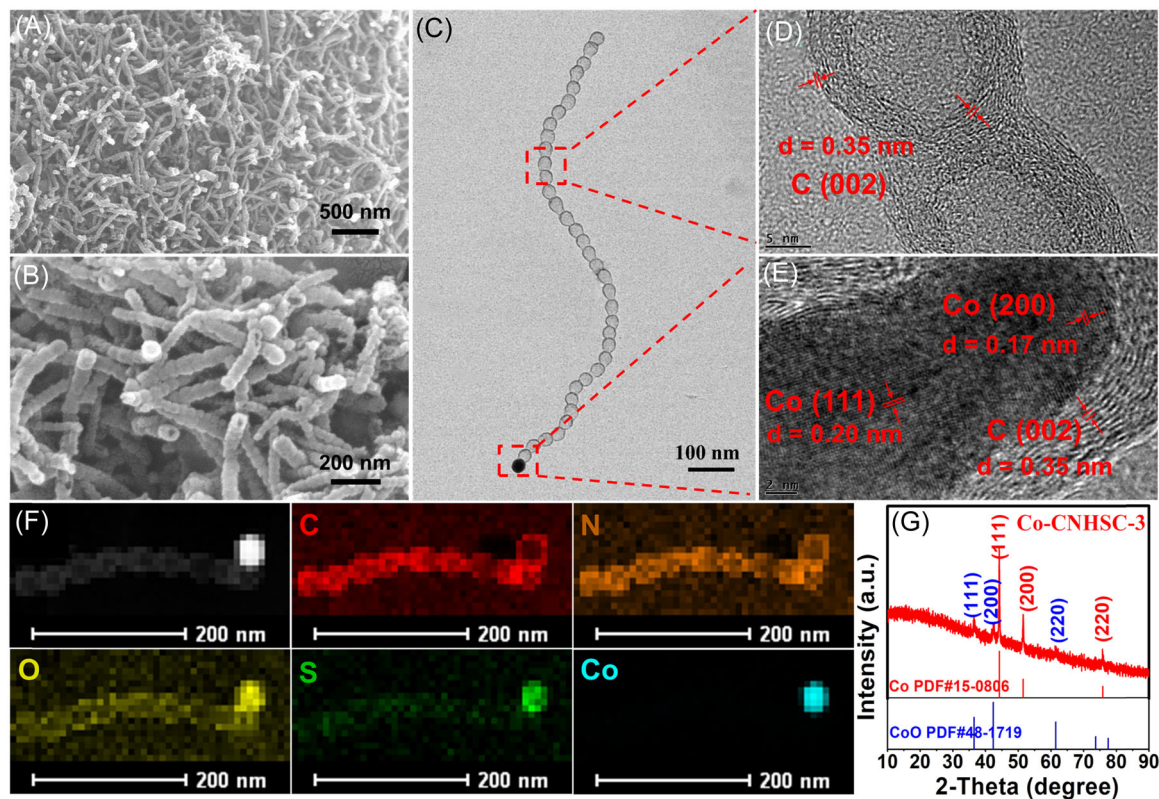


FIGURE 3 (A,B) SEM images at different magnifications of Co-CNHC-3. (C) TEM image and (D,E) HRTEM image of Co-CNHC-3. (F) HAADF-STEM image and the corresponding EDS elemental mapping images of C, N, O, S, and Co elements in Co-CNHC-3. (G) PXRD pattern of Co-CNHC-3.

indicate that it has an ultralong CNHSC. Its HRTEM images (Figure 3D,E) reveal that the wall of each hollow nanosphere is graphitic carbon with a lattice spacing of 0.35 nm, corresponding to the (002) plane of graphitic C, while the cobalt is encapsulated at one end of the nanosphere chain. The lattice fringes with d-spacings of 0.20 and 0.17 nm correspond to the (111) and (200) planes of Co, respectively. Furthermore, the homogeneous distribution of the C, N, O, S, and Co elements of Co-CNHS-3 was confirmed by the HAADF-STEM and the EDS mapping (Figure 3F). According to the EDS results (Figure S6), no Zn but only the above-mentioned elements were present, and Co was only located at one end of the chain.

PXRD analysis was performed to examine the structure of the as-prepared Co-CNHS-3. As shown in Figure 3G, the diffraction peaks located at 44.2°, 51.5°, and 75.9°, respectively, correspond to the (111), (200), and (220) planes of Co, consistent with the HRTEM. Moreover, three diffraction peaks with weaker absorption signals can be observed from the PXRD patterns. The three weak peaks at 36.5°, 42.4°, and 61.5° are assigned to the (111), (200), and (220) planes of CoO, respectively. This reveals that the material is mainly composed of metallic cobalt and a small amount of cobalt oxide. Figure S7 shows the PXRD patterns of the other catalysts reported in this article. It can be observed from the patterns that Co-BCNT-1 and Co-BCNT-2 without ZnSO₄ only contain Co.

Raman spectroscopy (Figure 4A) revealed that for all the samples in this work, a distinctive pair of D and G bands was observed at ca. 1340 and 1589 cm⁻¹, respectively, suggesting the existence of both disorder carbon and graphite carbon in the sample. Additionally, the integrated intensity ratio of the D to G peaks (I_D/I_G) is an indicator of the degree of disorder. The ratio is close to 1.11 for the sample Co-CNHS-3. The I_D/I_G value of the sample gets varied with the addition of ZnSO₄ (Figure S8A). The larger the I_D/I_G value, the greater the disorder of the graphitic carbon. An increase in the degree of disorder in the graphitic carbon means an increase in defects in the nanocomposite. Furthermore, the N₂ adsorption-desorption isotherms of all catalyst samples (Figure 4B) exhibit type IV adsorption isotherms with an H4-type hysteresis loop at a high relative pressure ($p/p_0 > 0.45$), demonstrating the excellent microporous structure of these samples. Among them, Co-CNHS-3 has the largest BET surface area (239.7 m² g⁻¹) (Figure S8B). The BJH pore diameter distribution (Figures 4B inset and S8C) of all the samples is between 0.5 and 1.0 nm, which again suggests that the catalysts possess a microporous structure. The high specific surface area and micro/mesoporous structure of Co-CNHS-3 not only provide abundant active sites but also guarantee the

accessibility of the reactants to the active sites, leading to the high observed electrocatalytic performance. FT-IR spectra were employed to further study the surface functional groups of these as-prepared samples. As shown in Figures 4C and S8D, they have three vibrational peaks, with the broadband at 3460 cm⁻¹ tentatively attributed to the ν -OH stretching vibrations in water molecules.⁴³ The peaks centered at 1120 cm⁻¹ are assigned to ν C-C vibrations. Notably, the peak at 1640 cm⁻¹ is attributed to the ν N-H vibration coupled with a ν C-N stretching mode,⁴⁴ demonstrating that the N atoms are well-doped into the samples. However, the ν C-S vibrations are not detectable due to the low content of S doping. Additionally, the ν C-O vibrations and ν C=O vibrations are also not found in the FT-IR spectrum,⁴³ indicating that there may be a very small amount of oxygen-containing functional groups in the carbon matrix.

XPS spectra were recorded to better understand the chemical composition and valence states of the related elements in these samples. The XPS results in Figures 4D and S9A confirmed the presence of C, O, N, S, and Co elements in the samples, in accordance with the elemental mapping results. Their high-resolution C 1s XPS spectra are presented in Figures 4E and S9B. There are four peaks at about 284.6, 285.2, 286.0, and 288.7 eV, corresponding to C-C sp³, C-C sp², C-N, and C-O, respectively. The formation of C-O bonds can be ascribed to the physically adsorbed oxygen on the graphene lattice.⁴⁰ Furthermore, the presence of C-N bonds indicates the successful doping of N into the carbon matrix.⁴⁵ Figures 4F and S9C show that the fitted peaks at 530.0 and 531.7 eV are related to O-Co and O-C, respectively. The broad peak at 533.5 eV is due to the presence of trace H₂O. In addition, the N 1s XPS spectra (Figures 4G and S9D) revealed four different N species at 398.4, 399.1, 400.3, and 401.4 eV, which are associated with pyridinic-N, pyrrolic-N, Co-N_x, and graphitic-N, respectively,⁴⁶ which confirms the presence of a considerable amount of N-doping in the supporting carbon structures. Notably, after the introduction of ZnSO₄, the content of pyridinic-N and pyrrolic-N in the catalyst increased significantly (Table S1). Based on reports published previously, the impact of the N-doping effect (pyridinic-N or pyrrolic-N) reflects a change in the electronic state and increased electron density allowing for electrocatalytic activity.⁴⁷ Furthermore, the S 2p spectra of the Co-CNHS-3-derived samples both contain two main peaks located at 163.9 and 165.3 eV, which are assigned to -C-S-C- S 2p_{3/2} and -C-S-C- S 2p_{1/2}, respectively. Another peak centered at 169.0 eV is ascribed to the -C-SO_x-C-sulfate species (Figure 4H).⁴⁸ However, the S 2p spectra of the

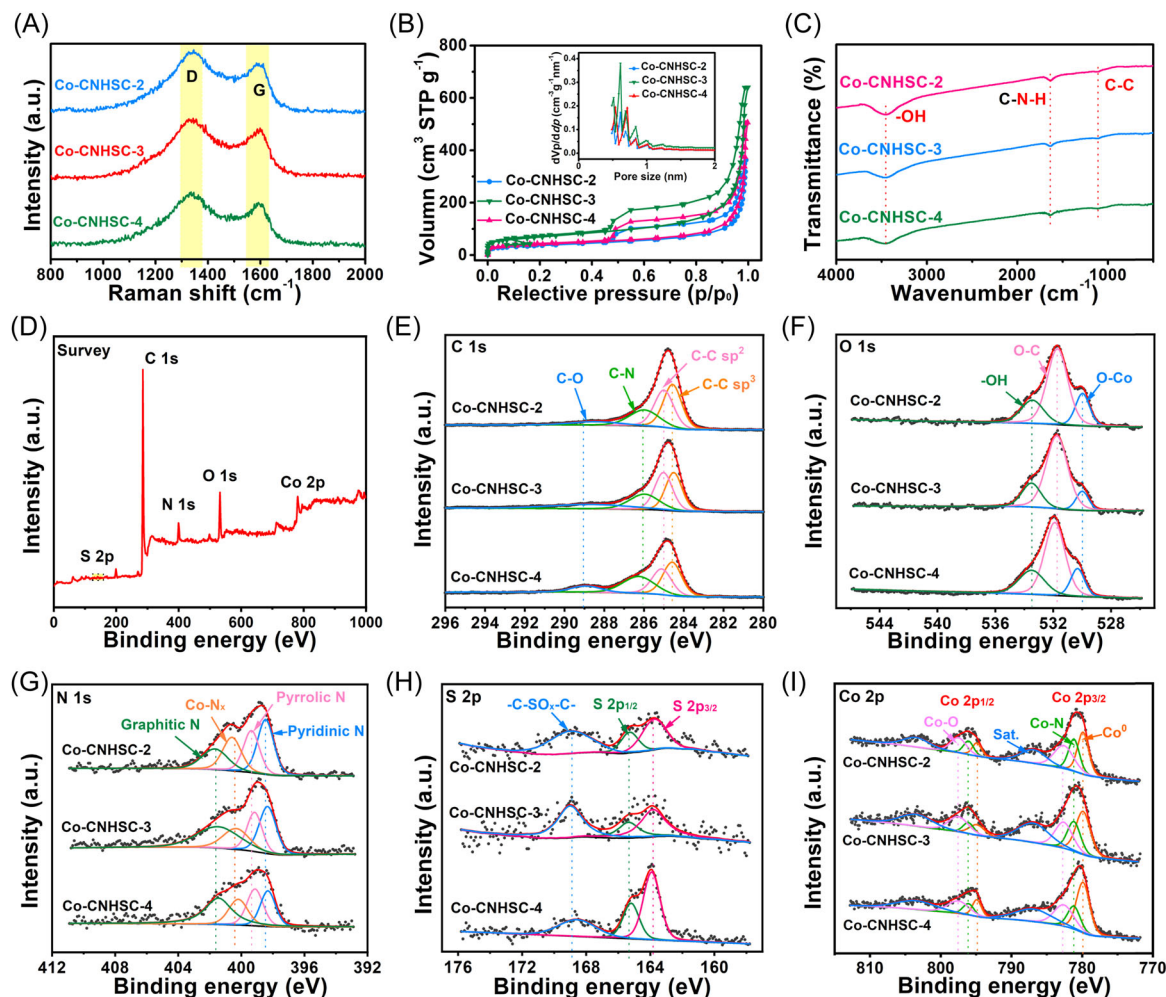


FIGURE 4 (A) Raman spectra, (B) nitrogen adsorption–desorption curve and corresponding pore size distribution diagram (inset), and (C) FT-IR spectra of Co-CNHSC-2, Co-CNHSC-3, and Co-CNHSC-4. (D) XPS survey spectrum of Co-CNHSC-3. (E–I) High-resolution XPS spectra of the C 1s, O 1s, N 1s, S 2p, and Co 2p of Co-CNHSC-2, Co-CNHSC-3, and Co-CNHSC-4.

Co-BCNT-derived samples possessed no absorption peak (Figure S9E). The difference between the S 2p spectra of Co-CNHSC and Co-BCNT confirms that S from sulfate is successfully doped into the carbon matrix (Table S2). For the Co 2p spectra (Figures 4I and S9F), the characteristic peak of Co^0 corresponding to Co NPs was observed at 779.8 and 794.8 eV. The peaks are located at 797.5 eV (Co 2p_{1/2}) and 781.6 eV (Co 2p_{3/2}) for Co^{2+} , while the other peaks are located at 795.8 eV (Co 2p_{1/2}) and 779.9 eV (Co 2p_{3/2}) are for Co^{3+} . Notably, the binding energies of 797.5 and 782.6 eV represent Co–O bonds,⁴⁹ which may be due to the fact that some Co NPs may be oxidized by air through surface defects in the carbon layer that wraps them. The binding energies of 796.1 eV and 781.1 eV may be related to the Co–N coordination due to nitrogen doping.³⁰ Furthermore, the binding energies for Co–S coordination are not found,^{50,51} indicating the absence of Co_xS_y in the samples. Additionally, the peaks around 803.4 and 786.8 eV are the two satellite peaks of Co.⁴⁹

The electrocatalytic performance of the as-prepared Co-CNHSC-3 composite for OER was investigated in 1 mol L⁻¹ KOH solution with a three-electrode system. For comparison, the Co-CNHSC-1/2/4, Co-BCNT-1/2, and RuO₂ were also assessed. Co-CNHSC-3 exhibits a better OER electrocatalytic activity with a low overpotential (1.58 V vs. RHE), which is close to that of RuO₂ (1.57 V) and outperforms those of other samples (Figure 5A). As shown in Figure 5B, the corresponding Tafel slope is 104.5 mV dec⁻¹ for Co-CNHSC-3, which is superior to those of recently reported cobalt-based OER catalysts.^{52,53} The detailed data for these materials are listed in Table S3. Apart from excellent catalytic activity, the stability in the OER procedure is also a crucial parameter for a practical electrocatalyst. Figure 5C shows that the LSV curve of the Co-CNHSC-3 composite after 500 CV cycles basically remained unchanged. Further, the Co-CNHSC-3 composite exhibits superior operational durability for OER activity over 60,000 s of continuous

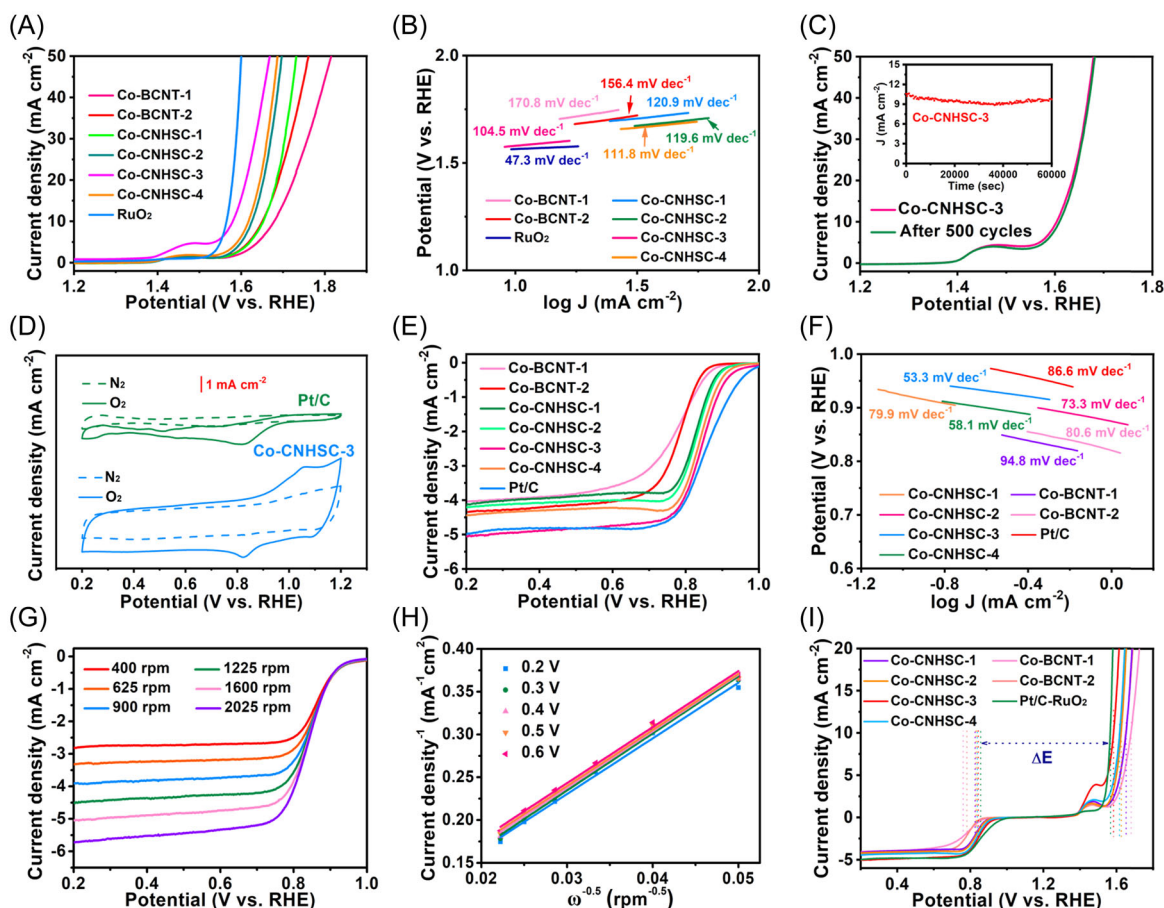


FIGURE 5 (A) LSV curves and (B) corresponding Tafel plots for RuO₂ and all samples for OER. (C) LSV curves of Co-CNHSC-3 before and after 500 CV cycles and the *i*-*t* plot at the applied potential of 1.5 V (vs. RHE) in 1.0 mol L⁻¹ KOH solution (inset). (D) CV curve of Pt/C and Co-CNHSC-3 at a scan rate of 50 mV s⁻¹ in N₂- and O₂-saturated 0.1 mol L⁻¹ KOH aqueous solution. (E) LSV curves of all catalysts at a scan rate of 5 mV s⁻¹ at a rotational speed of 1600 rpm. (F) Tafel plots obtained from the polarization curves in the acidic medium. (G) LSV curves for Co-CNHSC-3 at different rotation speeds. (H) K-L plots of Co-CNHSC-3 at different potentials from 0.2 V to 0.6 V. (I) Overall LSV curves for bifunctional activities to ORR and OER in 0.1 mol L⁻¹ KOH.

operation during chronoamperometry, exhibiting only a 4.7% decay in current density (Figure 5C inset). These results demonstrate the excellent stability of the Co-CNHSC-3 catalyst. Although the OER activity of Co-CNHSC-3 is slightly lower than that of RuO₂, it still outperforms some Co/carbon-based catalysts reported in the literature (Table S4).

To investigate the ORR catalytic activity of Co-CNHSC-3, CV measurements were examined in N₂- and then O₂-saturated 0.1 mol L⁻¹ KOH solution. As shown in Figure 5D, no obvious redox peaks were observed for Co-CNHSC-3 and Pt/C in N₂-saturated electrolytes. In contrast, when the electrolyte was saturated with O₂, pronounced oxygen reduction peaks were clearly observed at 0.83 V and 0.82 V for Co-CNHSC-3 and Pt/C, respectively. Moreover, after removing the background current, the Faradaic current density of the reduction peak of Co-CNHSC-3 (1.39 mA

cm⁻²) is slightly higher than that of Pt/C (1.24 mA cm⁻²), suggestive of better electrocatalytic activity.⁵⁴ LSV measurements were further used to investigate the electrocatalytic activity and kinetics of the Co-CNHSC-3 system and the other sample assemblies in the O₂-saturated electrolyte; the results are summarized in Table S5. The Co-CNHSC-3 composite (0.99 V) (Figure 5E) exhibits an onset potential (*E*_{onset}), comparable to the commercial Pt/C catalyst. In addition, the high half-wave potential (*E*_{1/2}) of 0.84 V is only about 10 mV lower than that of the commercial Pt/C, which is superior to those of most of the reported carbon-based catalysts.^{55,56} Figure 5F shows the Tafel slope, which is calculated from the ORR polarization curves. The Tafel slope of Co-CNHSC-3 is 53.3 mV dec⁻¹, which is lower than that of Pt/C (86.6 mV dec⁻¹), indicating its excellent catalytic activity. In addition, a comparison with recent works conducted on Co/carbon-based ORR catalysts is

given in Table S6. It is clear that the as-synthesized Co-CNHSC-3 exhibits good electrocatalytic performance in terms of onset and half-wave potential, Tafel slope, and so forth. The linear and parallel K-L plots (Figure 5H) derived from LSV curves at different speeds of 400–2500 rpm (Figure 5G) reflect a first-order reaction with respect to the dissolved O_2 . The electron transfer number (n) for Co-CNHSC-3 is calculated at ~ 4.0 over the potential range 0.2–0.6 V based on K-L plots, confirming an apparent $4e^-$ pathway to reduce O_2 into OH^- .⁵⁷ The overpotential difference (ΔE , the difference between the overpotential of OER at a current density of 10 mA cm^{-2} and the half-wave potential of ORR) is generally used to evaluate the overall activity of a bifunctional catalyst. A better bifunctional catalyst tends to have a smaller ΔE value. As shown in Figure 5I, Co-CNHSC-3 exhibits a low ΔE value of 0.74 V, which is close to that of the benchmark Pt/C-RuO₂ catalysts (0.72 V) and outperforms those of other catalysts, indicating better bifunctional performance. The detailed data of ΔE for these materials are listed in Table S7.

Electrochemical surface areas (ECSAs) were calculated to further analyze the electrochemical performance of all the samples. The double-layer capacitance (C_{dl}) values, which are calculated from CV curves at different scan rates (Figure S10), were executed to verify the ECSA of the catalysts.⁵⁸ Figure 6A shows that under ORR conditions, the Co-CNHSC-3 electrode displayed the largest C_{dl} value (12.1 mF cm^{-2}) among all the catalysts. Thus, the Co-CNHSC-3 composite has the largest ECSA at 302.5 cm^2 (Figure 6B), suggesting that it has more active sites for ORR compared with the other catalysts. All C_{dl} values and ECSA are shown in Table S7. Electrochemical impedance spectroscopy (EIS) analyses, which provide the charge-transfer resistance (R_{ct}) of the synthesized catalysts, were conducted to provide insight into the electrode kinetics. The Co-CNHSC-3 composite exhibits the lowest R_{ct} values among the six samples (Figure 6C), indicating that there is a faster charge transfer rate during the ORR reaction. The above results demonstrate that excellent electrical conductivity and a large electrochemical area are beneficial for improving the high catalytic performance of the Co-CNHSC-3.

Long-term stability measurements on Co-CNHSC-3 and Pt/C were evaluated by CV and current–time ($i-t$) chronoamperometric experiments. Figure 6D shows that the LSV curve of the Co-CNHSC-3 almost coincides with the initial curve after 500 cycles in an alkaline solution. Furthermore, after the durability test was performed over 30,000 s, approximately 94.4% of the initial current density of the Co-CNHSC-3 remained, whereas for the Pt/C catalyst, only 57.1% of the initial current density was observed after 25,000 s (Figure 6E). In addition, the

Co-CNHSC-3 also exhibited excellent tolerance to methanol. When 3 mol L^{-1} methanol was injected into the electrolyte after approximately 600 s, the current density of the Co-CNHSC-3 remained substantially unchanged with a current retention of $\sim 100\%$ after 3000 s (Figure 6F). On the contrary, the current density of commercial Pt/C decreased sharply with a current retention of 50.8% after 2600 s, due to the onset of methanol oxidation. The above results indicate that Co-CNHSC-3, which has excellent stability and methanol tolerance, is an excellent carbon-based catalyst suitable for fuel cells. Moreover, to further examine the stability of the catalyst after the long-term operation, TEM, XRD, and XPS were performed after 500 cycles in the potential regions associated with the OER or ORR (Figures S11–S13). These findings suggested that the Co-CNHSC-3 catalyst, with its excellent stability, can be used for long-term practical applications.

To confirm the active sites of Co-CNHSC-3, we immersed it in 3 mol L^{-1} H_2SO_4 solution for 6 h to remove Co NPs at the tip of the chain according to the synthesis method of M-N-C catalysts.^{59,60} As shown in Figure S14, these Co NPs disappeared and the morphology of the acid-washed Co-CNHSC-3 did not change, but its OER and ORR activities decreased significantly. The results suggested that the possibility of single-atom cobalt sites on the surface of each carbon nano-hollow-sphere could be ruled out and the main active sites should be N,S co-doped carbon-coated Co NPs. Therefore, to further explore the interaction between the carbon layer and Co NPs and the effect of N and S doping, we performed DFT simulations using VASP software. In accordance with previous analysis results, we choose the ORR process as the analysis model. According to the physical characterization results, a defective N,S co-doped graphene layer at the Co (111) crystal plane (denoted as NSC-Co) was established to verify the synergistic ORR catalysis of the Co NPs and the N,S-doped graphene (Figures S15A and S16). For comparison, configurations for Co (111) supported N-doped graphene (denoted as NC-Co) were also constructed (Figures S15B and S17). Figure 7A shows a plot of the four elementary reaction steps: (1) OOH formation: $* + O_2 + H_2O + e^- \rightarrow OOH* + OH^-$; (2) OOH dissociation: $OOH* + e^- \rightarrow O* + OH^-$; (3) O hydration: $O* + H_2O + e^- \rightarrow OH* + OH^-$; and (4) OH desorption: $OH* + e^- \rightarrow * + OH^-$, with calculated Gibbs free energy profiles at $U = 0$, where the asterisk represents the adsorption site.⁶¹ From the calculation of free energy, it is clear that the rate determination step for both NSC-Co and NC-Co is $* + O_2 + H_2O + e^- \rightarrow OOH* + OH^-$. The corresponding maximum free energy changes are calculated to be 0.78 and 0.81 eV at 0 V, indicating that the NSC-Co surface exhibits a lower activation energy and superior ORR

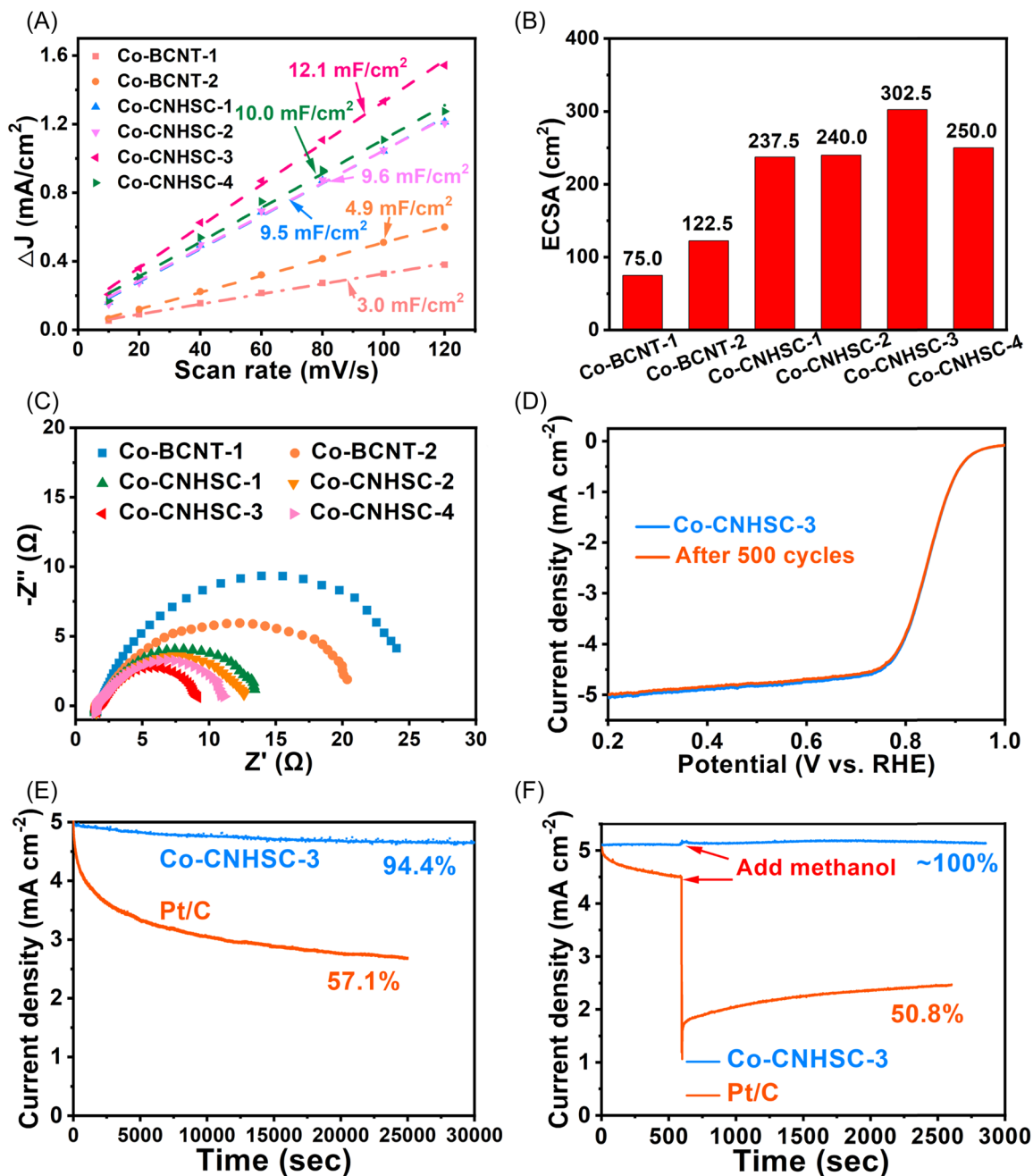


FIGURE 6 (A) Measured capacitive currents plotted as a function of the scan rate of all catalysts measured at 0.15 V versus RHE. (B) Histogram of the electrochemically active area of all catalysts. (C) EIS spectra of all catalysts. (D) LSV curves of Co-CNHSC-3 before and after 500 cycles. (E) Durability of Co-CNHSC-3. (F) Methanol crossover effect test of Co-CNHSC-3.

catalytic efficiency than the NC-Co sites and that the NSC-Co interface is more inclined to the four-electron reaction pathway. In addition, the difference between charge density and the Bader charge in the rate-determination step and the adsorption energy of intermediates during the reaction process were also calculated to further analyze the excellent electrocatalytic performance of the Co-CNHSC catalyst. The difference in charge density of NC-Co and NSC-Co is shown in Figure 7B,C, respectively, where the yellow represents the charge

accumulation and the blue represents the charge depletion. It is clear that the NSC-Co model has a higher charge density and more obvious electron gain and loss, which further indicates that heteroatom doping can adjust the electronic structure to form active centers, and that N,S co-doping is better than N doping. Moreover, Bader charge analysis (Table S8) also reveals that NSC-Co (0.55) has a higher electron density than NC-Co (0.48), indicative of a higher binding energy, which is consistent with the analysis of charge density

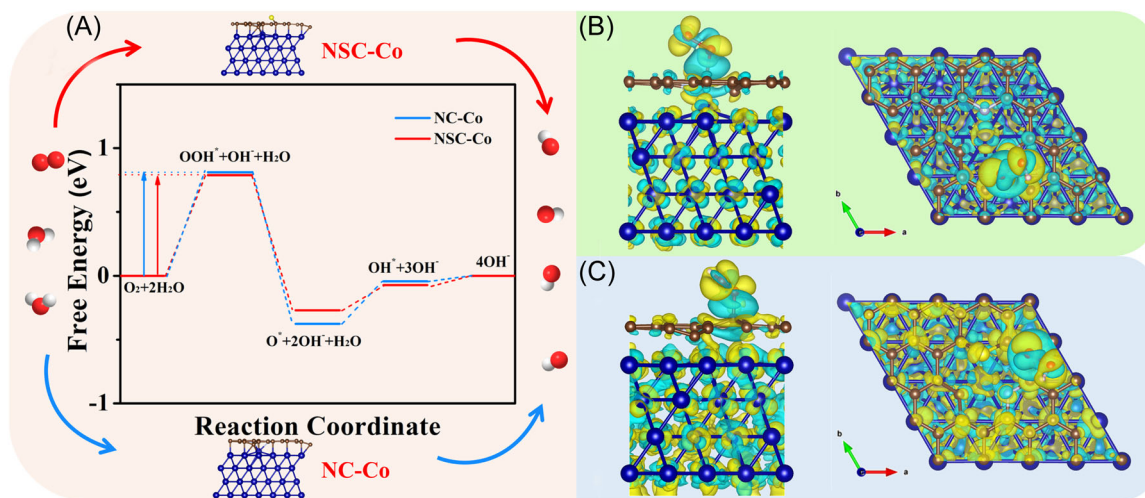


FIGURE 7 (A) Free-energy diagram of ORR on NSC-Co and NC-Co electrodes. (B,C) Charge density differences of the carbon layer in the catalyst models of NC-Co and NSC-Co, in which the Co, C, S, and N atoms are in blue, gray, yellow, and light white, respectively; the yellow and light blue areas represent charge accumulation and depletion, respectively.

difference.⁶² In summary, DFT calculations demonstrate that N,S co-doping not only changes the electronic structure of the carbon layer to create more catalytically active centers, but also the electron transfer between N,S and metallic Co further tunes the carbon layer's charge density, which is favorable for the electron balance of the adsorbed O atoms on the Co-CNHSC catalyst.

Rechargeable zinc-air batteries (ZABs) are regarded as one of the most promising high-efficiency and eco-friendly energy technologies and one of the important methods for evaluating the electrochemical performance of the catalysts.⁵⁵ Based on the excellent ORR and OER catalytic activity and stability of Co-CNHSC-3 under alkaline conditions, a rechargeable ZAB was assembled with Co-CNHSC-3 as the air electrode catalyst to evaluate its electrochemical performance and potential application. For comparison, a Pt/C-RuO₂-based ZAB was also constructed and tested under the same operating conditions.⁶³ A zinc plate and 6 mol L⁻¹ KOH with 0.2 mol L⁻¹ zinc acetate solution were used as the anode and electrolyte (Figure 8A). The assembled battery affords a high open circuit voltage of 1.425 V (Figure 8B), slightly higher than that of Pt/C-RuO₂ (1.413 V). The discharge polarization curves and the corresponding power density plots are shown in Figure 8C. The peak power density of the Co-CNHSC-3 is calculated to be 118.1 mW cm⁻², which is higher than that of Pt/C-RuO₂ (82.5 mW cm⁻²). As revealed in the charge-discharge polarization curves (Figure 8D), the Co-CNHSC-3 exhibits a much lower voltage gap compared to the counterpart Pt/C-RuO₂ catalysts, indicating its excellent rechargeability when used as an oxygen electrode bifunctional catalyst in Zn-air batteries. Additionally, according to the mass of Zn

consumed, the specific capacity of the ZAB using Co-CNHSC-3 is up to 1023.6 mAh g_{Zn}⁻¹ at a current density of 10 mA cm⁻², superior to that of the Pt/C-RuO₂ catalyst (857.0 mAh g_{Zn}⁻¹) and those of the recently reported transition metal/carbon-based catalysts,⁶⁴⁻⁶⁶ indicating a higher utilization of zinc (Figure 8E). More importantly, the long-term stability experiment (Figure 8F) shows that Co-CNHSC-3 exhibits excellent stability with only about 3.6% voltage loss after 30 h at a discharge current density of 10 mA cm⁻². In addition, Co-CNHSC-3 has a higher voltage (1.277 V), superior to the Pt/C-RuO₂ catalyst (1.073 V). Furthermore, the rate discharge performance in Figure 8G shows that the two battery systems behave similarly with a tendency to higher discharge currents resulting in lower voltage output. It is worth noting that the discharging potentials of Zn-air batteries are above 1.15 V at 50 mA cm⁻², higher than that of the Pt/C-RuO₂ catalyst (1.10 V), suggesting a good rate performance for the Co-CNHSC-3 composites. Furthermore, the cycling stability of the Zn-air battery was evaluated by galvanostatic discharge and charge at 10 mA cm⁻² (Figure 8H). Notably, after 200 continuous charge/discharge cycles (about 80 h), the voltage gap of the Co-CNHSC-3 catalyst remained almost unchanged with well-retained energy efficiency of over 50%. By contrast, a distinct deterioration is observed for the Pt/C-RuO₂ catalyst over a shorter cycling period (100 cycles, about 40 h). These results indicate the enhanced cycling stability associated with the Co-CNHSC-3 electrode. The preminent discharging capability and cycling performance of the Zn-air battery equipped with Co-CNHSC-3 are comparable with or even better than those of reported advanced bifunctional catalysts (Table S9).

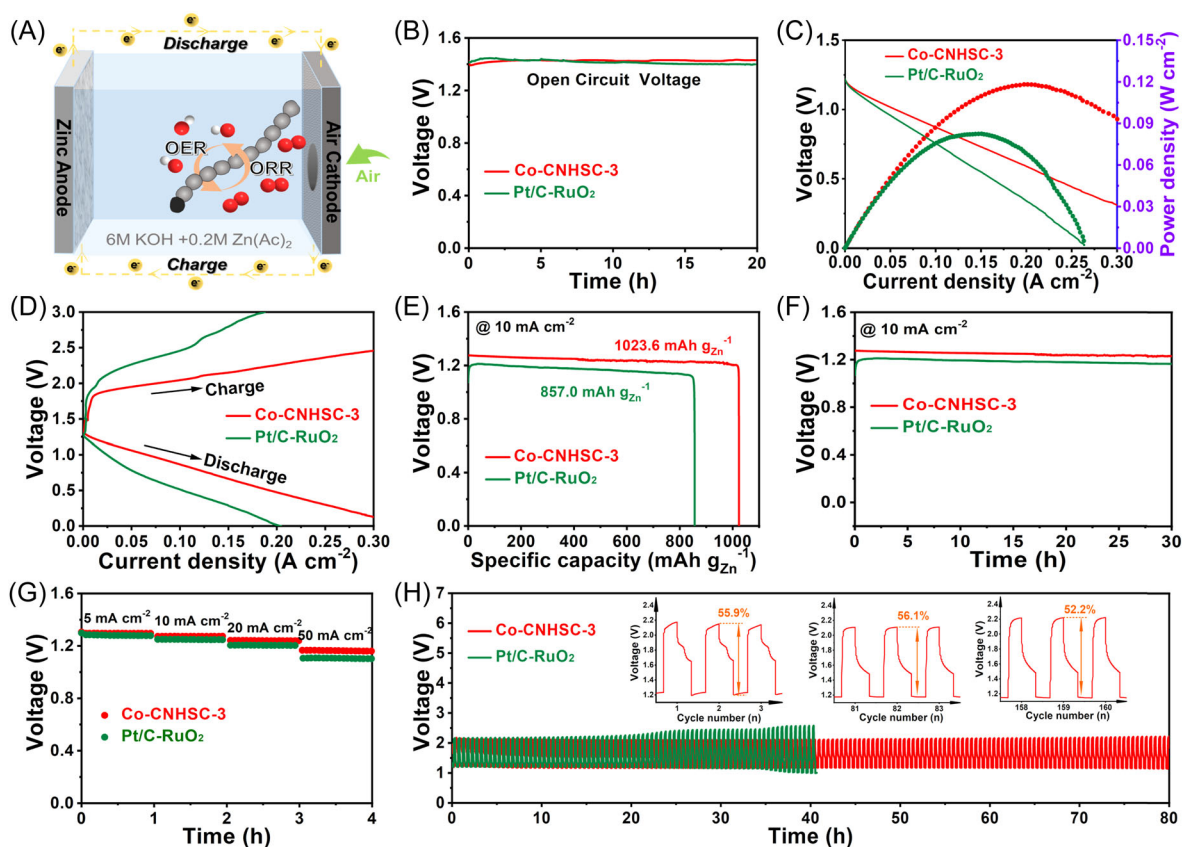


FIGURE 8 (A) Schematic illustration of the liquid Zn-air battery. (B) Open circuit voltage plots and (C) discharge polarization curve and corresponding power density of Zn-air batteries. (D) Discharge and charge polarization curves using Co-CNHSC-3 and Pt/C-RuO₂ as air catalysts. (E) Specific capacities of the Zn-air batteries using Co-CNHSC-3 and Pt/C-RuO₂ as ORR catalysts normalized to the mass of the consumed Zn. (F) Long-term galvanostatic discharge curves of Zn-air batteries using Co-CNHSC-3 and Pt/C-RuO₂ as air catalysts at 10 mA cm⁻². (G) Discharge profiles of the Zn-air batteries using Co-CNHSC-3 and Pt/C-RuO₂ as the air catalysts from low current density to high current density (5, 10, 20, and 50 mA cm⁻²). (H) Discharge-charge cycling curves of the Zn-air battery based on Co-CNHSC-3 and Pt/C-RuO₂ as the bifunctional air electrodes at a current density of 10 mA cm⁻².

4 | CONCLUSION

In conclusion, we have developed an efficient and facile process for the in situ synthesis of ultralong N,S co-doped carbon nano-hollow-sphere chains with encapsulated Co NPs (Co-CNHSCs), which is currently the longest CNHSC with a length of about 1300 nm. Moreover, the Co-CNHSC catalysts exhibited desirable bifunctional catalytic activity for ORR and OER, of which the catalyst Co-CNHSC-3 is the most preferred. More importantly, the catalyst also showed a robust performance when used in rechargeable Zn-air batteries, which can be attributed to the following structural and compositional advantages: (i) The ultralong CNHSCs structure can serve as a high conductive scaffold, which is conducive to mass-charge transmission; (ii) The larger specific surface area brought about by the porous structure can provide more accessible active sites to adsorb O₂; (iii) The introduction of Co, N, and S modulated the electronic structure of the

carbon substrate, which improved the interaction between the catalyst surface and generated O intermediates; (iv) The catalysts gather numerous efficient active species, including active centers formed by the N and S doping-induced charge redistribution and Co and Co-N_x brought about by the introduction of Co. The synergy between these active species promotes the electrochemical processes. Therefore, this work provides a new perspective on the design of efficient and cost-effective multifunctional carbon-based catalysts for energy conversion.

ACKNOWLEDGMENTS

The authors thank the National Natural Science Foundation of China (22271203 and 21773163), the State Key Laboratory of Organometallic Chemistry of Shanghai Institute of Organic Chemistry (KF2021005), the Collaborative Innovation Center of Suzhou Nano Science and Technology, the Priority Academic Program Development

of Jiangsu Higher Education Institutions, and the Project of Scientific and Technologic Infrastructure of Suzhou (SZS201905). CR thanks the EPSRC for an Overseas Travel Grant (EP/R023816/1). The authors are grateful for the useful comments and suggestions of the editor and the reviewers.

CONFLICT OF INTEREST

The authors declare that there are no conflict of interests.

ORCID

Jian-Ping Lang  <http://orcid.org/0000-0003-2942-7385>

REFERENCES

- Leong KW, Wang Y, Ni M, Pan W, Luo S, Leung DYC. Rechargeable Zn-air batteries: recent trends and future perspectives. *Renew Sustain Energy Rev.* 2022;154:111771.
- Yuan S, Duan X, Liu J, et al. Recent progress on transition metal oxides as advanced materials for energy conversion and storage. *Energy Stor Mater.* 2021;42:317-369.
- Zhang Q, Wang C, Xie Z, Zhou Z. Defective/doped graphene-based materials as cathodes for metal-air batteries. *Energy Environ Mater.* 2022;5(4):1103-1116.
- Yang D, Chen D, Jiang Y, et al. Carbon-based materials for all-solid-state zinc-air batteries. *Carbon Energy.* 2021;3(1):50-65.
- Tian Y, Xu L, Li M, et al. Correction to: interface engineering of CoS/CoO@N-doped graphene nanocomposite for high-performance rechargeable Zn-air batteries. *Nano-Micro Lett.* 2021;13(1):97.
- Niu Y, Gong S, Liu X, et al. Engineering iron-group bimetallic nanotubes as efficient bifunctional oxygen electrocatalysts for flexible Zn-air batteries. *eScience.* 2022;2(5):546-556.
- Han X, Ling X, Yu D, et al. Atomically dispersed binary Co-Ni sites in nitrogen-doped hollow carbon nanocubes for reversible oxygen reduction and evolution. *Adv Mater.* 2019;31(49):1905622.
- Li Y, Sun Y, Qin Y, et al. Recent advances on water-splitting electrocatalysis mediated by noble-metal-based nanostructured materials. *Adv Energy Mater.* 2020;10(11):1903120.
- Du Y, Sheng H, Astruc D, Zhu M. Atomically precise noble metal nanoclusters as efficient catalysts: a bridge between structure and properties. *Chem Rev.* 2020;120(2):526-622.
- Yang H, Liu Y, Liu X, et al. Large-scale synthesis of N-doped carbon capsules supporting atomically dispersed iron for efficient oxygen reduction reaction electrocatalysis. *eScience.* 2022;2(2):227-234.
- Zhao T, Wang Y, Karuturi S, Catchpole K, Zhang Q, Zhao C. Design and operando/in situ characterization of precious-metal-free electrocatalysts for alkaline water splitting. *Carbon Energy.* 2020;2(4):582-613.
- Du L, Zhang G, Liu X, et al. Biomass-derived nonprecious metal catalysts for oxygen reduction reaction: the demand-oriented engineering of active sites and structures. *Carbon Energy.* 2020;2(4):561-581.
- Paul R, Du F, Dai L, et al. 3D heteroatom-doped carbon nanomaterials as multifunctional metal-free catalysts for integrated energy devices. *Adv Mater.* 2019;31(13):1805598.
- Qiang F, Feng J, Wang H, et al. Oxygen engineering enables N-doped porous carbon nanofibers as oxygen reduction/evolution reaction electrocatalysts for flexible zinc-air batteries. *ACS Catal.* 2022;12(7):4002-4015.
- Guo B, Ma R, Li Z, et al. Hierarchical N-doped porous carbons for Zn-air batteries and supercapacitors. *Nano-Micro Lett.* 2020;12(1):20.
- Masood ul Hasan I, Peng L, Mao J, et al. Carbon-based metal-free catalysts for electrochemical CO₂ reduction: activity, selectivity, and stability. *Carbon Energy.* 2021;3(1):24-49.
- Aoki K, Senga R, Suga Y, et al. Structural analysis and oxygen reduction reaction activity in bamboo-like nitrogen-doped carbon nanotubes containing localized nitrogen in nodal regions. *Carbon.* 2017;123:99-105.
- Jiao Y, Zheng Y, Davey K, Qiao SZ. Activity origin and catalyst design principles for electrocatalytic hydrogen evolution on heteroatom-doped graphene. *Nat Energy.* 2016;1(10):16130.
- Li J, Zhang Y, Zhang X, et al. S, N dual-doped graphene-like carbon nanosheets as efficient oxygen reduction reaction electrocatalysts. *ACS Appl Mater Interfaces.* 2017;9(1):398-405.
- Zhang Z, Sun J, Dou M, Ji J, Wang F. Nitrogen and phosphorus codoped mesoporous carbon derived from polypyrrole as superior metal-free electrocatalyst toward the oxygen reduction reaction. *ACS Appl Mater Interfaces.* 2017;9(19):16236-16242.
- Quílez-Bermejo J, Morallón E, Cazorla-Amorós D. Metal-free heteroatom-doped carbon-based catalysts for ORR: a critical assessment about the role of heteroatoms. *Carbon.* 2020;165:434-454.
- Xiao J, Han J, Zhang C, Ling G, Kang F, Yang QH. Dimensionality, function and performance of carbon materials in energy storage devices. *Adv Energy Mater.* 2022;12(4):2100775.
- Wu M, Liao J, Yu L, et al. Roadmap on carbon materials for energy storage and conversion. *Chem Asian J.* 2020;15(7):995-1013.
- Arshad A, Yun S, Shi J, Sun M, Zafar N, Hagfeldt A. N-coordinated bimetallic defect-rich nanocarbons as highly efficient electrocatalysts in advanced energy conversion applications. *Chem Eng J.* 2022;435(2):134913.
- Wu ZP, Zhang H, Zuo S, et al. Manipulating the local coordination and electronic structures for efficient electrocatalytic oxygen evolution. *Adv Mater.* 2021;33(40):2103004.
- Jiang H, Xia J, Jiao L, et al. Ni single atoms anchored on N-doped carbon nanosheets as bifunctional electrocatalysts for urea-assisted rechargeable Zn-air batteries. *Appl Catal B.* 2022;310:121352.
- Sui S, Wang X, Zhou X, Su Y, Riffat S, Liu C. A comprehensive review of Pt electrocatalysts for the oxygen reduction reaction: nanostructure, activity, mechanism and carbon support in PEM fuel cells. *J Mater Chem A.* 2017;5(5):1808-1825.
- Ji H, Wang M, Liu S, et al. In-situ observation as activity descriptor enables rational design of oxygen reduction catalyst for zinc-air battery. *Energy Storage Mater.* 2020;27:226-231.
- Macedo Andrade A, Liu Z, Grewal S, et al. MOF-derived Co/Cu-embedded N-doped carbon for trifunctional ORR/OER/HER catalysis in alkaline media. *Dalton Trans.* 2021;50(16):5473-5482.
- Ge H, Li G, Shen J, Ma W, Meng X, Xu L. Co₄N nanoparticles encapsulated in N-doped carbon box as tri-functional catalyst

- for Zn-air battery and overall water splitting. *Appl Catal B*. 2020;275:119104.
31. Wang B, Tang J, Zhang X, et al. Nitrogen doped porous carbon polyhedral supported Fe and Ni dual-metal single-atomic catalysts: template-free and metal ligand-free synthesis with microwave-assistance and d-band center modulating for boosted ORR catalysis in zinc-air batteries. *Chem Eng J*. 2022;437(1):135295.
 32. Singh TI, Maibam A, Cha DC, et al. High-alkaline water-splitting activity of mesoporous 3D heterostructures: an amorphous-shell@crystalline-core nano-assembly of Co-Ni-phosphate ultrathin-nanosheets and V-doped cobalt-nitride nanowires. *Adv Sci*. 2022;9(23):2201311.
 33. Kong F, Cui X, Huang Y, et al. N-doped carbon electrocatalyst: marked ORR activity in acidic media without the contribution from metal sites? *Angew Chem Int Ed*. 2022;61(15):e2021162.
 34. Kresse G, Furthmüller J. Efficiency of ab-initio total energy calculations for metals and semiconductors using a plane-wave basis set. *Comput Mater Sci*. 1996;6(1):15-50.
 35. Kresse G, Joubert D. From ultrasoft pseudopotentials to the projector augmented-wave method. *Phys Rev B*. 1999;59(3):1758-1775.
 36. Blöchl PE. Projector augmented-wave method. *Phys Rev B*. 1994;50(24):17953-17979.
 37. Zhang X, Zhang Q, Cui J, Yan J, Liu J, Wu Y. New insights into the key bifunctional role of sulfur in Fe-N-C single-atom catalysts for ORR/OER. *Nanoscale*. 2022;14(8):3212-3223.
 38. Ying Y, Fan K, Luo X, Qiao J, Huang H. Unravelling the origin of bifunctional OER/ORR activity for single-atom catalysts supported on C₂N by DFT and machine learning. *J Mater Chem A*. 2021;9(31):16860-16867.
 39. Lin M, Tan JPY, Boothroyd C, Loh KP, Tok ES, Foo YL. Dynamical observation of bamboo-like carbon nanotube growth. *Nano Lett*. 2007;7(8):2234-2238.
 40. Ashok A, Kumar A, Ponraj J, Mansour SA. Synthesis and growth mechanism of bamboo like N-doped CNT/graphene nanostructure incorporated with hybrid metal nanoparticles for overall water splitting. *Carbon*. 2020;170:452-463.
 41. Wu S, Yi F, Ping D, et al. Constructing single-atomic nickel sites in carbon nanotubes for efficient CO₂ electroreduction. *Carbon*. 2022;196:1-9.
 42. Zhou X, Leng X, Ling C, Chong H, Xu AW, Yang Z. Integrating a metal framework with Co-confined carbon nanotubes as trifunctional electrocatalysts to boost electron and mass transfer approaching practical applications. *Nanoscale*. 2021;13(29):12651-12658.
 43. Bin Q, Lin B, Zhu K, et al. Superior trichloroethylene removal from water by sulfide-modified nanoscale zero-valent iron/graphene aerogel composite. *J Environ Sci*. 2020;88:90-102.
 44. Yao Y, Lian C, Wu G, et al. Synthesis of "sea urchin"-like carbon nanotubes/porous carbon superstructures derived from waste biomass for treatment of various contaminants. *Appl Catal B*. 2017;219:563-571.
 45. Chai L, Hu Z, Wang X, et al. Fe₇C₃ nanoparticles with in situ grown CNT on nitrogen doped hollow carbon cube with greatly enhanced conductivity and ORR performance for alkaline fuel cell. *Carbon*. 2021;174:531-539.
 46. Shu X, Chen S, Chen S, Pan W, Zhang J. Cobalt nitride embedded holey N-doped graphene as advanced bifunctional electrocatalysts for Zn-Air batteries and overall water splitting. *Carbon*. 2020;157:234-243.
 47. Liu P, Gao D, Xiao W, et al. Self-powered water-splitting devices by core-shell NiFe@N-graphite-based Zn-air batteries. *Adv Funct Mater*. 2018;28(14):1706928.
 48. Liu F, Shi L, Song S, et al. Simultaneously engineering the coordination environment and pore architecture of metal-organic framework-derived single-atomic iron catalysts for ultraefficient oxygen reduction. *Small*. 2021;17(40):2102425.
 49. Yang L, Huang N, Luo C, et al. Atomically dispersed and nanoscaled Co species embedded in micro-/mesoporous carbon nanosheet/nanotube architecture with enhanced oxygen reduction and evolution bifunction for Zn-Air batteries. *Chem Eng J*. 2021;404:127112.
 50. Wang Y, Wu X, Jiang X, et al. Citrulline-induced mesoporous CoS/CoO heterojunction nanorods triggering high-efficiency oxygen electrocatalysis in solid-state Zn-air batteries. *Chem Eng J*. 2022;434:134744.
 51. Fang Z, Qi J, Xu Y, et al. Promoted generation of singlet oxygen by hollow-shell CoS/g-C₃N₄ catalyst for sulfonamides degradation. *Chem Eng J*. 2022;441:136051.
 52. Wang Y, Yu H, Zhu L, et al. Cytosine-Co assemblies derived CoN_x rich Co-NCNT as efficient tri-functional electrocatalyst. *J Colloid Interface Sci*. 2021;585:276-286.
 53. Zhang J, Zhang T, Ma J, Wang Z, Liu J, Gong X. ORR and OER of Co-N codoped carbon-based electrocatalysts enhanced by boundary layer oxygen molecules transfer. *Carbon*. 2021;172:556-568.
 54. Alshehri SM, Alhabarah AN, Ahmed J, Naushad M, Ahamad T. An efficient and cost-effective tri-functional electrocatalyst based on cobalt ferrite embedded nitrogen doped carbon. *J Colloid Interface Sci*. 2018;514:1-9.
 55. Wang T, He Y, Liu Y, et al. A ZIF-triggered rapid polymerization of dopamine renders Co/N-codoped cage-in-cage porous carbon for highly efficient oxygen reduction and evolution. *Nano Energy*. 2021;79:105487.
 56. Peng W, Yang X, Mao L, et al. ZIF-67-derived Co nanoparticles anchored in N doped hollow carbon nanofibers as bifunctional oxygen electrocatalysts. *Chem Eng J*. 2021;407:127157.
 57. Zhong Y, Pan Z, Wang X, et al. Hierarchical Co₃O₄ nano-micro arrays featuring superior activity as cathode in a flexible and rechargeable zinc-air battery. *Adv Sci*. 2019;6(11):1802243.
 58. Singh H, Marley-Hines M, Chakravarty S, Nath M. Multi-walled carbon nanotube supported manganese selenide as a highly active bifunctional OER and ORR electrocatalyst. *J Mater Chem A*. 2022;10(12):6772-6784.
 59. Ding R, Chen Y, Li X, et al. Atomically dispersed, low-coordinate Co-N sites on carbon nanotubes as inexpensive and efficient electrocatalysts for hydrogen evolution. *Small*. 2022;18(4):2105335.
 60. Liu W, Zhang C, Zhang J, et al. Tuning the atomic configuration of Co-N-C electrocatalyst enables highly-selective H₂O₂ production in acidic media. *Appl Catal B*. 2022;310:121312.
 61. Yang CC, Zai SF, Zhou YT, Du L, Jiang Q. Fe₃C-Co nanoparticles encapsulated in a hierarchical structure of N-doped carbon as a multifunctional electrocatalyst for

- ORR, OER, and HER. *Adv Funct Mater.* 2019;29(27): 1901949.
62. Cheng Y, Gong J, Cao B, et al. Ultrafine VN nanodots induced generation of abundant cobalt single-atom active sites on nitrogen-doped carbon nanotube for efficient hydrogen evolution. *J Energy Chem.* 2022;68:646-657.
63. Zhou Q, Hou S, Cheng Y, et al. Interfacial engineering Co and MnO within N,S co-doped carbon hierarchical branched superstructures toward high-efficiency electrocatalytic oxygen reduction for robust Zn-air batteries. *Appl Catal B.* 2021; 295:120281.
64. Jose V, Hu H, Edison E, et al. Modulation of single atomic Co and Fe sites on hollow carbon nanospheres as oxygen electrodes for rechargeable Zn-air batteries. *Small Methods.* 2021;5(2):2000751.
65. Li J, Kang Y, Wei W, Li X, Lei Z, Liu P. Well-dispersed ultrafine CoFe nanoalloy decorated N-doped hollow carbon microspheres for rechargeable/flexible Zn-air batteries. *Chem Eng J.* 2021;407:127961.
66. Wu K, Zhang L, Yuan Y, et al. An iron-decorated carbon aerogel for rechargeable flow and flexible Zn-air batteries. *Adv Mater.* 2020;32(32):2002292.

SUPPORTING INFORMATION

Additional supporting information can be found online in the Supporting Information section at the end of this article.

How to cite this article: Zhang W, Guo X, Li C, et al. Ultralong nitrogen/sulfur Co-doped carbon nano-hollow-sphere chains with encapsulated cobalt nanoparticles for highly efficient oxygen electrocatalysis. *Carbon Energy.* 2023;1-16. doi:10.1002/cey2.317